

Predicting unsteady flow separation in response to a flow disturbance

Karen Mulleners* and Julien Deparday[†] and Guosheng He[‡] and Sabrina Henne[§]
École polytechnique fédérale de Lausanne, 1015 Lausanne, Switzerland

We present here a summary of the activities and results of dynamically stalling airfoils from the UNFoLD lab at EPFL that have been presented at the meetings of the NATO AVT-282 discussion group on *Unsteady aerodynamic response of rigid wings in gust encounters* during the past three years. The results are based on experimental data for a sinusoidally pitching OA209 airfoil in a wind tunnel at $Re = 9.2 \times 10^5$, a sinusoidally pitching NACA0015 airfoil profile with a trailing edge flap in a wind tunnel at $Re = 5.5 \times 10^5$, and a sharp-edged flat plate undergoing a ramp-up motion in a recirculating water channel at $Re = 77\,500$. The first two data sets are used to study the onset of dynamic stall and the third one is used to analyse post-stall load fluctuations. Based on the experimental data, we derived a new model of the leading edge suction parameter that accurately predicts the value and the timing of the maximum leading edge suction and dynamic stall onset on a pitching airfoil. The model is based on thin airfoil theory and links the evolution of the leading edge suction and the shear layer during stall development. By including an oscillating trailing edge flap, the lift polars can be significantly altered but the dynamic stall time delay is only marginally affected by the kinematics of the flap. The maximum lift coefficient is strongly affected by both the main wing and the trailing edge flap kinematics. For a flat plate without flap, the maximum lift coefficient and the subsequent post stall peak values increase with increasing pitch rate up to a critical pitch rate beyond which the entire lift response become independent of the pitch rate. The convective time delay to reach the primary lift peak decreases with increasing pitch rate up to the critical pitch rate and the time delay between subsequent peaks slightly decreases until the limit cycle oscillation period is reached.

I. Introduction

UNSTEADY flow separation or dynamic stall occurs on lifting profiles subjected to an unsteady increase in angle of attack beyond the static stall angle. The increase in angle of attack can be the result of a prescribed motion of the blades or due to the encounter of a flow disturbance or gust [1–3]. Among the characteristic features associated with dynamic stall are the delay of flow separation beyond the static stall angle and a lift overshoot. Although stall delay and lift overshoot sound beneficial, dynamic stall is generally a phenomenon that is to be avoided. Large excursions of the highly unsteady aerodynamic loads following stall onset decrease the aerodynamic efficiency and yield strong vibrations and increasing structural forces and bending moments that cause fatigue and potential damage to the airfoil and the structure supporting it [4–6]. To protect the integrity of the airfoil and the supporting structure and avoid loss of aerodynamic performance, it is essential to accurately predict the dynamic stall development, onset, and post-stall behaviour.

In this contribution, we present results from our lab that are deemed of interest for the NATO AVT-282 discussion group on *Unsteady aerodynamic response of rigid wings in gust encounters*. Our contributions include results of water channel and wind tunnel experiments with airfoil profiles that are subjected to pitch angle variations leading to flow separation. All experiments combine velocity field measurements with airfoil surface pressure or force measurements. The water channel experiments are conducted with a sharp edges flat plate subjected to a linear ramp-up motion. The wind tunnel experiments are conducted with a two dimensional OA209 airfoil and a NACA0015 airfoil profile that is equipped with a trailing edge flap. The trailing edge flap is dynamically pitched to mimic the effect of a flow disturbance. In all cases,

* Assistant professor, EPFL-STI-IGM-UNFoLD, Station 9, CH-1015 Lausanne, Switzerland. Senior Member AIAA.

[†] Post-doctoral researcher, EPFL-STI-IGM-UNFoLD, Station 9, CH-1015 Lausanne, Switzerland.

[‡] Post-doctoral researcher, EPFL-STI-IGM-UNFoLD, Station 9, CH-1015 Lausanne, Switzerland.

[§] PhD candidate, EPFL-STI-IGM-UNFoLD, Station 9, CH-1015 Lausanne, Switzerland.

we analyse the time-resolved flow development in response to the disturbance and focus on the reaction time scales as a function of the characteristic parameters describing the disturbance.

The goal of the different experiments is to identify dynamic stall prediction parameters that have critical values at dynamic stall onset that are largely independent of the flow and motion conditions or that can easily be predicted or derived for various flow disturbances.

II. Experimental set-ups and methods

Three sets of experiments are highlighted in this paper:

- a sinusoidally pitching OA209 airfoil in a wind tunnel at $Re = 9.2 \times 10^5$,
- a sinusoidally pitching NACA0015 airfoil profile with a trailing edge flap in a wind tunnel at $Re = 5.5 \times 10^5$, and
- a sharp-edged flat plate undergoing a ramp-up motion in a recirculating water channel at $Re = 77\,500$.

A. Sinusoidally pitching OA209 airfoil at $Re = 9.2 \times 10^5$

This experimental data has been used for various in-depth analyses on the onset and development of dynamic stall [7–10]. The experiments were conducted in a closed-circuit, low-speed wind tunnel of the German Aerospace Centre (DLR) in Göttingen. The wind tunnel had an open test section with a rectangular nozzle measuring $0.75\text{ m} \times 1.05\text{ m}$. The experiments included synchronised unsteady surface pressure and time-resolved particle image velocimetry (TR-PIV) in the vertical plan and mid-span for a sinusoidally pitching OA209 airfoil. The model had a chord length of $c = 0.3\text{ m}$ and was placed in a uniform flow of $U_\infty = 50\text{ m/s}$ which correspond to a Reynolds number of $Re = 9.2 \times 10^5$. The unsteady pressure distribution was determined using a series of 41 surface-mounted pressure transducers, which were sampled at a rate of 6 kHz and integrated to obtain the lift history. The TR-PIV data were evaluated using a multigrid algorithm with a final interrogation window size of $32\text{ px} \times 32\text{ px}$ and an overlap of approximately 80 %. The velocity field was measured with a spatial resolution of 1.2 mm, or $0.004c$, at an acquisition rate of 1500 Hz. The airfoil was sinusoidally oscillated around its quarter-chord location. The mean incidence angle α_0 , amplitude α_1 , and oscillation frequency f_{osc} have been varied to obtain a wide range of dynamic stall cycles with reduced frequencies $k = \pi f_{osc} c / U_\infty$ varying between 0.05 to 0.1. To better describe the influence of the unsteadiness of a sinusoidal pitching motion on dynamic stall development, we have previously introduced the instantaneous effective unsteadiness $\dot{\alpha}_{ss} c / U_\infty$, which is defined as the rate of change of the angle of attack at the moment when the static stall angle is exceeded, non-dimensionalised by the convective time.

B. Sinusoidally pitching NACA0015 airfoil with an oscillating trailing-edge flap at $Re = 5.5 \times 10^5$

More recently, we obtained experimental data on a pitching NACA0015 airfoil with an oscillating trailing-edge flap. The trailing edge flap is dynamically pitched to mimic the effect of a flow disturbance. The airfoil was mounted into the same closed-circuit, low-speed wind tunnel of the German Aerospace Centre that was used for the first data set. This time, the incoming free stream velocity was at $U_\infty = 30\text{ m/s}$. The chord length was $c = 0.3\text{ m}$, leading to a Reynolds number based on the chord of $Re = 5.5 \times 10^5$.

The airfoil was pitched around the quarter chord axis and had a movable trailing edge flap with the rotation axis at $0.7c$. The movement of the main airfoil and of the flap were actuated by servomotors and could be independently controlled. The main airfoil was pitched around the static stall angle of attack $\alpha_0 = 20^\circ$ with an amplitude of $\alpha_1 = 8^\circ$ and frequency of f_{osc} . The reduced frequency k for the main airfoil ranges from 0.025 to 0.15. The flap was either deflected at a fixed angle $\beta_0 \in \{-20^\circ, -10^\circ, 0^\circ, 10^\circ, 20^\circ\}$ or oscillated around the symmetrical plane at $\beta_0 = 0^\circ$ with an amplitude of $\beta_1 = 20^\circ$. A phase shift ϕ between the sinusoidal oscillation of the main airfoil and the flap was varied. The variation of the phase shift was deemed to influence the leading edge stagnation point while keeping the geometric leading edge motion constant. The objective of these measurements was to characterise the role and the interplay between the leading edge suction and the leading edge stagnation point during dynamic stall.

The airfoil surface pressure distribution was measured using 36 pressure transducers integrated in the model mid-span cross section. Lift and pitching moment histories were obtained by integration of the pressure distribution around the airfoil. The sampling rate for the pressure measurement was 20 kHz.

Two-dimensional TR-PIV was used to measure the flow field in the vertical plane at the model mid-span. The flow field was illuminated by a dual-pulsed laser and the particle images were recorded by two PCO DIMAX HS cameras with $1800\text{ px} \times 1600\text{ px}$ sensors. The first camera was zoomed in near the leading edge and the second camera had a larger field of view covering the rest of the airfoil. The sampling rate for the PIV was 1.5 kHz. A multi-grid algorithm was

used to obtain the velocity vectors with a final window size of $48 \text{ px} \times 48 \text{ px}$ and 50 % overlap.

C. Sharp-edged flat plate undergoing a ramp-up motion at $\text{Re} = 77\,500$

To focus on the load fluctuation and following dynamic stall onset, we conducted these experiments in the SHARX recirculating water channel at EPFL. The facility has a $0.6 \text{ m} \times 0.6 \text{ m} \times 3.0 \text{ m}$ test section and can reach a free-stream velocity $U_\infty = 1 \text{ m/s}$. A sharp-edged flat plate of chord length $c = 0.15 \text{ m}$ and span $s = 0.6 \text{ m}$ (aspect ratio $AR = s/c = 4$) was placed at the centre of the test section. The plate was made from plexiglass and was suspended vertically in the channel, with a minimal gap between the tip and the lower wall of the channel in order to minimise tip effects. The upper tip extended above the free surface to serve as the mounting point for the flat plate airfoil.

The airfoil was actuated to undergo a ramp motion, moving from an angle of attack $\alpha = 0^\circ$ to $\alpha = 30^\circ$ at a constant pitch rate. The dimensionless pitch rate $\dot{\alpha}c/U_\infty$ was varied from 0.75 to 7.5. The chord Reynolds number was $\mathcal{R} = 77\,500$. Time-resolved PIV was used to measure the velocity field around and behind the airfoil. Two high-speed cameras with $1024 \text{ px} \times 1024 \text{ px}$ sensors (Photron, ILA 5150 GmbH), were placed side by side to cover a region of interest including the airfoil and the wake. A double cavity diode pumped Nd:YLF laser ($\lambda = 527 \text{ nm}$) with a maximum pulse energy of 30 mJ was used to create the laser sheet. The light sheet was oriented horizontally at a distance of 0.2 m from the bottom of the water channel to reduce the influence of the free surface. For every ramp up motion, we recorded 10 000 images at an acquisition rate of 500 Hz yielding a total measurement time of 20 s. The measurement series covers the initial ramp-up motion and the transient decay of the flow to a quasi-steady state. The images were processed for both cameras separately according to standard procedures, with the multi-grid algorithm with image deformation, a final window size of $64 \text{ px} \times 64 \text{ px}$, and an overlap of 50 %.

A NEMA17 stepper motor geared at a ratio of 1:25 rotated the plate about its quarter-chord position. The shaft was connected directly to a 6-component ATI load cell, which served as the interface between the motor and the airfoil to enable direct measurement of hydrodynamic forces. The load data was recorded with a sampling frequency of 1 kHz, a sensing range of 125 N, and a resolution of 0.02 N.

III. Results and discussion

A. Dynamic stall on a sinusoidally pitching OA209 airfoil at $\text{Re} = 9.2 \times 10^5$

The typical response of the flow to a sinusoidal pitching measured by simultaneous unsteady surface pressure and time-resolved velocity field measurements is presented in figure 1. The flow initially remains attached during the pitch-up motion even when the angle of attack is larger than the static stall angle. The resulting lift coefficient is larger than for a steady case. Figure 1 presents the time evolution of the lift coefficient during one oscillating period T , as well as according to the associated angle of attack α and the convective time t^* . The static stall angle is reached at t_{ss} . When the static stall is exceeded, the lift keeps increasing but at a lower rate than before t_{ss} . During this period, the flow is attached at the leading edge and starts to detach near the trailing edge (figure 1 a. and b.). This is the first stage of the dynamic stall development (light shading in figure 1) as defined in [8, 10]. Later during the pitch-up motion, counter clockwise vorticity appears between the shear layer and the suction side of the wing. The shear layer starts to roll up into a large scale dynamic stall vortex (figure 1 c.). The lift coefficient is decreasing even though the angle of attack continues to be increased. The stage that is dominated by the formation of the dynamic stall vortex (dark shading in figure 1) ends when the dynamic stall vortex detaches from the airfoil (figure 1 d.) and is shed downstream. After these two stages describing the dynamic stall development, the flow is completely detached and the wing experiences a significant decrease of the lift coefficient with large variations of loads during the end of the pitch-up motion and during the pitch-down motion until the flow reattaches (figure 1 f.).

The lift overshoot before the unsteady detached phase is a typical response of a pitching motion, which is described by the two-stage dynamic stall development. The duration of the first stage decreases linearly with the unsteadiness of the pitching motion, which can be quantified by the normalised effective unsteadiness $\dot{\alpha}_{ss}c/U_\infty$. The duration of the second stage, about four times shorter than the first stage, is independent of the normalised effective unsteadiness. The two-stage dynamic stall development was independently confirmed by global velocity field and local surface pressure measurements around the leading edge.

The leading edge pressure signals for the sinusoidally pitching airfoil at $\text{Re} = 9.2 \times 10^5$ were combined into a single leading edge suction parameter and we recently developed an improved model of the leading edge suction parameter based on thin airfoil theory. Thin airfoil theory determines the aerodynamic force on an airfoil as the result of the

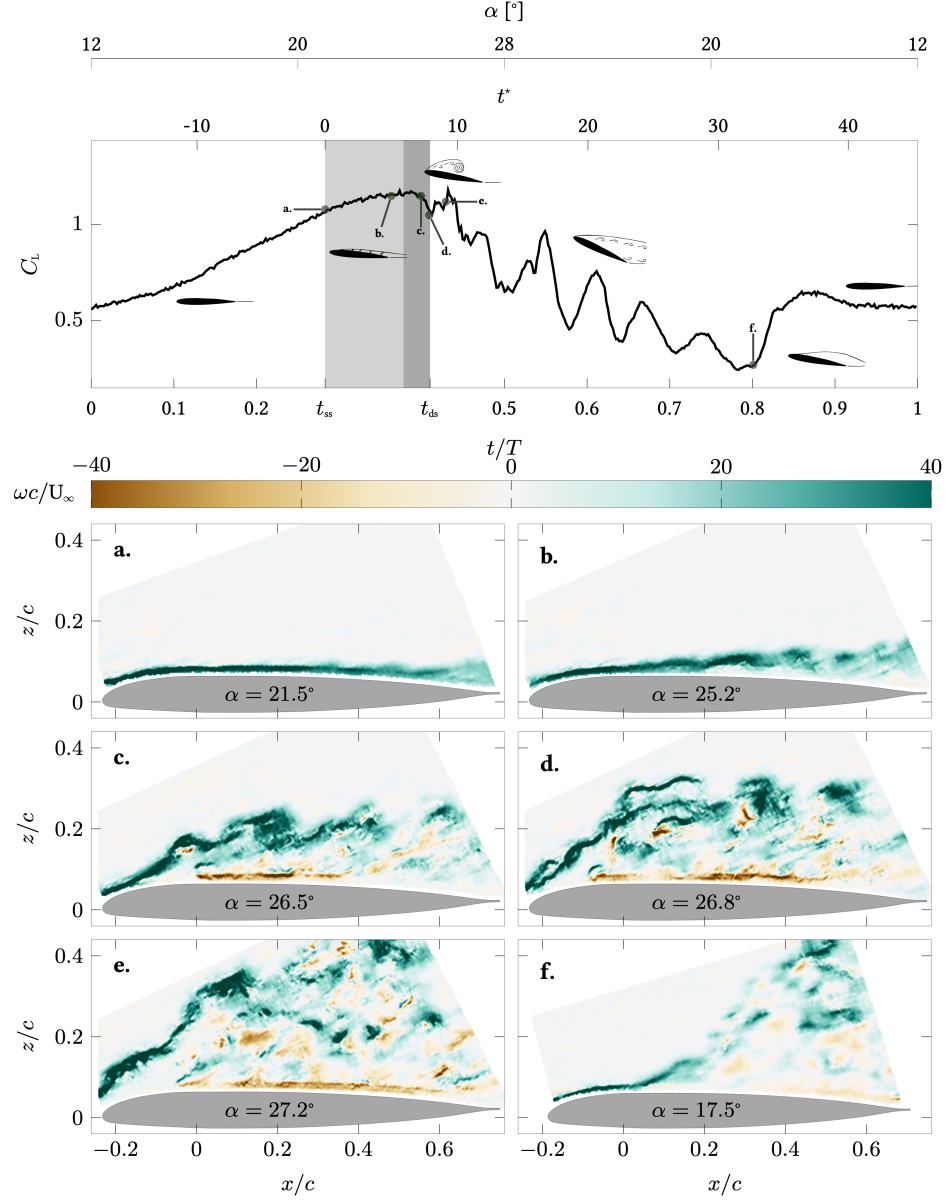


Figure 1 Temporal evolution of the lift coefficient during a single pitching cycle described by $\alpha_0 = 20^\circ$, $\alpha_1 = 8^\circ$, $k = 0.05$, and $\dot{\alpha}_{ss}c/U_\infty = 0.013$. The labels a. to f. in the lift history indicate the timing of the velocity and vorticity field snapshots. The shaded regions refer to the stall development stages between the time when the static stall angle of attack is exceeded t_{ss} and the dynamic stall onset is reached t_{ds} .

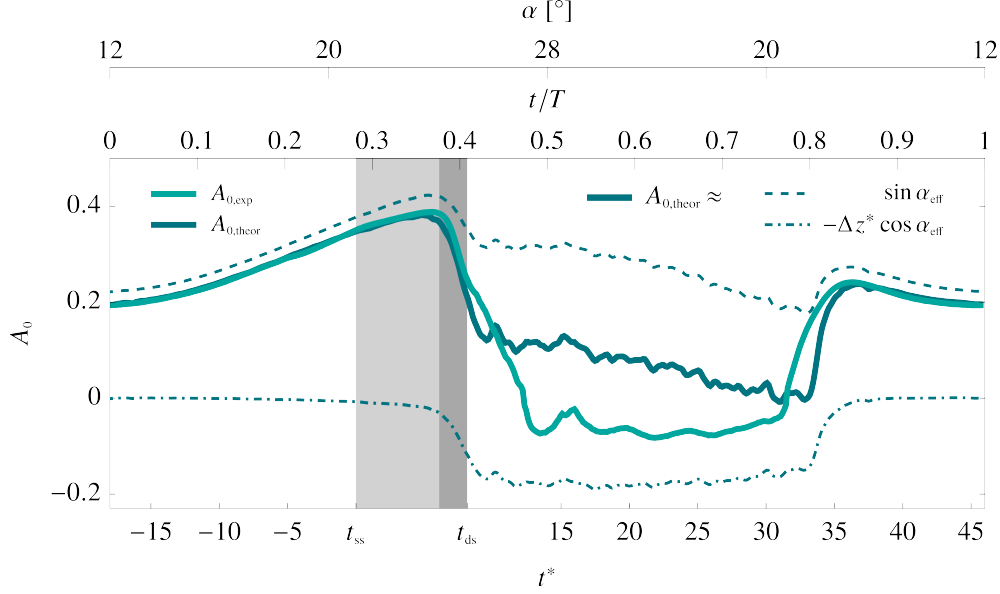


Figure 2 Comparison of the experimental phase-averaged leading edge suction parameter ($A_{0,exp}$) and the modified theoretical model ($A_{0,theor}$) for a pitching motion described by $\alpha_0 = 20^\circ$, $\alpha_1 = 8^\circ$, $k = 0.05$, and $\dot{\alpha}_{ss}c/U_\infty = 0.013$. The modified model takes into account the twofold influence of the shear layer on the effective angle of attack and the effective camber presented by dashed lines.

potential pressure field induced by a vortex sheet [11]. The circulation distribution for a generalised camber line can be described as a Fourier series. The first Fourier coefficient A_0 represents the leading edge suction peak resulting from the acceleration of the flow around the airfoil's leading edge and is called the leading edge suction parameter [12, 13]. The leading edge suction parameter can also be determined experimentally from the pressure at the leading edge. We have recently proposed an improved model of this leading edge suction parameter based on thin airfoil theory and linking the evolution of the leading edge suction and the shear layer growth during stall development [10]. The influence of the growth of the shear layer during dynamic stall development on the flow around the airfoil is described in terms of an increase of the effective camber and a decrease of the effective angle of attack of the airfoil. The effective angle of attack is defined as:

$$\alpha_{eff} = \alpha - \tan \Delta z^* \quad (1)$$

with Δz^* the experimentally determined dimensionless chord-wise average of the shear layer height. The effective camber of the virtually altered airfoil profile due to the presence of the shear layer is expressed as:

$$K_{\eta_{eff}} = K_\eta + \Delta z^* \quad (2)$$

with K_η the original geometric camber line. By taking into account this twofold influence of the shear layer development, our new model of the leading edge suction parameter reads:

$$A_{0,theor'} = \sin \alpha_{eff} + \dot{\alpha} \frac{c}{4U} - K_\eta \cos \alpha_{eff} - \Delta z^* \cos \alpha_{eff} . \quad (3)$$

This modified model accurately predicts the value and the timing of the maximum leading edge suction on the pitching airfoil (figure 2).

B. Dynamic stall on a sinusoidally pitching NACA0015 airfoil with a trailing-edge flap at $Re = 5.5 \times 10^5$

The typical response of the flow to the sinusoidal pitching of the NACA0015 with the trailing edge flap fixed at $\beta_0 = \beta_1 = 0^\circ$ is similar to the response described in the previous section. The lift polar for the fixed, non-deviated flap presented in the left panel of figure 3 has the same characteristic features as the lift polar for the thinner, non-symmetric OA209 presented in the previous section. The lift coefficient increases linearly during most of the pitch-up part of the

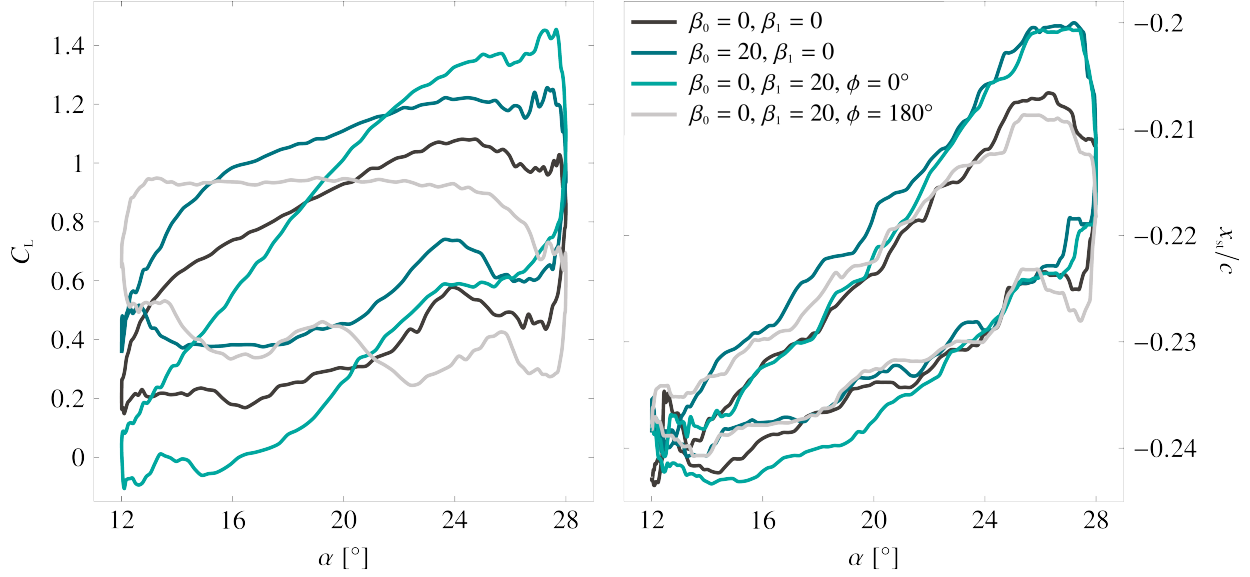


Figure 3 Lift coefficient and stagnation point as a function of angle of attack α of the main airfoil during a single pitching cycle for the various configurations of the trailing edge flap where β_0 refers to the mean flap angle with respect to the chord length, β_1 refers to the flap amplitude, and ϕ refers to the phase difference between the sinusoidal pitching of the main airfoil and the flap.

cycle beyond the static stall angle of $\alpha_{ss} = 20^\circ$. Stall is delayed to a higher angle of attack and there is a significant lift overshoot with respect to the maximum statically attainable lift coefficient. The maximum lift coefficient is reached around $\alpha = 24^\circ$. After reaching the global lift maximum, the shear layer starts to roll-up and the lift coefficient drops until the first stall vortex is shed and the lift increases again before reaching the maximum angle of attack. During the pitch-down part of the cycle, the lift drops rapidly and strong fluctuations are observed that can be directly linked to the formation and shedding of subsequent large scale vortices.

The corresponding evolution of the stream-wise position of the leading edge stagnation point during the selected pitching cycle is presented in the right panel of figure 3. The stagnation point is located on the pressure surface of the airfoil during the entire pitching cycle and its stream-wise position was directly extracted from the velocity field measurements in the leading edge region. More specifically, it was identified as the extrapolated intersection of the ridge in the positive time FTLE that indicates the leading edge stagnation line with the airfoil surface. This is indicated in figure 4 where we show an instantaneous snapshot of the velocity field obtained from the camera with the leading edge field of view. In addition to the velocity vectors, the scalar positive-time FTLE is colour coded.

The FTLE is a scalar measure of the local maximum rate of separation over an integration time T . The FTLE at a spatial location x_0 , at a time instant t_0 is defined as

$$FTLE(x_0, t_0, T) = \frac{1}{2T} \log \sigma(x_0, t_0)$$

with σ the coefficient of expansion which is defined as the maximum eigenvalue of the Cauchy-Green strain tensor or

$$\sigma(x_0, t_0, T) = \lambda_{\max} \left(\left[\frac{\partial \chi(x_0, t_0, T)}{\partial x_0} \right]^t \left[\frac{\partial \chi(x_0, t_0, T)}{\partial x_0} \right] \right)$$

with λ_{\max} the maximum Lyapunov exponent and $\chi(x_0, t_0, T)$ the flow map over the integration time T . The Cauchy-Green tensor is the spatial gradient of the flow map. Regions of localised material stretching generate local maxima in the FTLE.

With increasing angle of attack, the stagnation point moves downstream, i.e. towards the trailing edge, until it reaches a maximum values for $\alpha \approx 24^\circ$, when the lift reaches its maximum value as well. Thereafter, the stagnation point gradually moves back to its initial most upstream location at which it was at the start of the pitch-up (figure 3, right). By deviating the trailing flap to a fixed angle $\beta_0 = 20^\circ$, the entire lift polar is shifted up by a constant amount of $\Delta C_L \approx 0.15$ (figure 3, left). When the flow is attached, this is exactly what we would expect as the fixed flap deviation

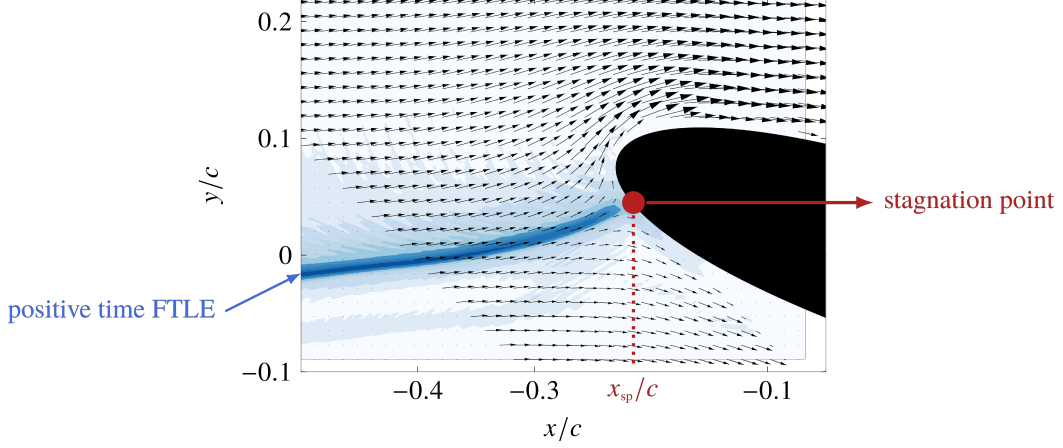


Figure 4 Instantaneous snapshot of the velocity field in the leading edge region of the airfoil. In addition to the velocity vectors, the positive time FTLE is colour coded to indicate the leading edge stagnation line.

increases the effective camber of the airfoil. During this attached flow portion of the cycle, the leading edge stagnation point is also shifted downstream on the pressure surface by a nearly constant amount with respect to the stagnation point location for the oscillation with a fixed, non-deviated flap (figure 3, right). After dynamic stall onset, the stagnation point moves back upstream and follows the same position evolution as it does for the non-deviated flap configuration. Once the flow fully stalls the stagnation point location is no longer influenced by the deviation of the flap, but the lift coefficient remains larger than the for the non-deviated flap configuration by approximately the same amount as during the attached flow stage (figure 3, left).

When the flap is oscillated in phase with the main airfoil ($\phi = 0^\circ$), the dynamic stall lift polar curve seems to be rotated (figure 3, left). It reaches an even larger maximum lift than for the configuration with the flap fixed at $\beta_0 = 20^\circ$ even though their instantaneous geometry at maximum angle of attack is the same. This indicates that the instantaneous effective geometrical angle of attack is not sufficient to predict the lift coefficient and the time history of the flap

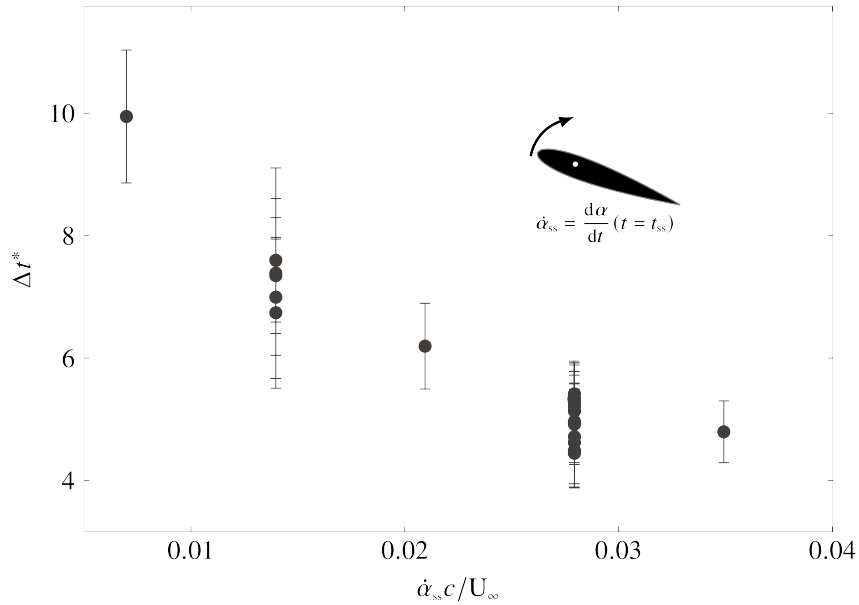


Figure 5 Dynamic stall delay for various combinations of trailing edge flap pitching kinematics for sinusoidal oscillations of the main wing around $\alpha_0 = 20^\circ$ with an amplitude $\alpha_1 = 8^\circ$ for various reduced frequencies. The stall delay is plotted as a function of the instantaneous effective unsteadiness.

kinematics need to be taken into account. The stagnation point location on the other hand seems to be mainly influenced by the effective geometric angle of attack during the attached flow stage (figure 3, right).

When the flap is oscillated out of phase with the main airfoil ($\phi = 180^\circ$), the dynamic stall lift polar curve seems to be further rotated (figure 3, left) such that the lift coefficient during most of the pitch-up motion is approximately constant. The timing at which the lift drops due to massive flow separation does not seem to be affected when compared with the other configurations.

The variations in stall delay for various pitching kinematics of the trailing edge flap and various reduced frequencies of the main airfoil oscillations are summarised in figure 5. The stall delay was calculated here as the convective time delay between the point at which the static stall angle of attack was exceeded and the occurrence of the first local minimum after the maximum lift coefficient. We have shown in the previous section, that the first local minimum corresponds to the shedding of the primary dynamic stall vortex and stall onset. The stall delay is plotted as a function of the instantaneous effective unsteadiness which describes well the influence of the unsteadiness of a sinusoidal pitching motion on dynamic stall development. In accordance with previous results [7] the dynamic stall delay decreases with increasing unsteadiness and the trailing edge flap kinematics seem to have very little effect on the stall delay.

C. Dynamic stall on a sharp-edged flat plate undergoing a ramp-up motion at $Re = 77\,500$

A flat plate subjected to quick ramp-up motion from $\alpha = 0^\circ$ up to $\alpha = 30^\circ$ at a Reynolds number $Re = 77\,500$ with varying pitch rates was investigated to analyse in more detail the post stall load fluctuations. The lift responses for various motions with different dimensionless pitch rates ($\dot{\alpha}c/U_\infty$) are presented in figure 6. In general, the lift increases more or less linearly over time until it reaches a maximum value which is higher than the lift coefficient associated with a static flat plate at $\alpha = 30^\circ$. After reaching the maximum value, the lift coefficients oscillate around a slowly decreasing value that converges towards the steady state value. For the range of experiments conducted, we observe up to three clearly distinguishable lift peaks that are directly linked to the growth and separation of three successive leading edge vortices. For $\dot{\alpha}c/U_\infty > 4$ the lift curves exhibit an additional peak before the actual global maximum is reached, which is due to the added mass effect.

The initially increasing slope of the lift coefficients becomes steeper with increasing pitch rate and the various load oscillations become more pronounced. The higher the pitch rate $\dot{\alpha}c/U_\infty$, the closer the lift curves become and they completely overlap for the highest investigated dimensionless pitch rates. The magnitude of the three local lift maxima initially increases with dimensionless pitch rate and they all reach constant critical values for $\dot{\alpha}c/U_\infty > \approx 3$ (section C). The convective time between the start of the motion and the time at which the first maximum is reached decreases initially with dimensionless pitch rate until it reaches an approximately constant value of 5 for $\dot{\alpha}c/U_\infty > 3$ (figure 8). For higher pitch rates, higher levels of vorticity are generated. This leads to stronger vortices that separate earlier than at

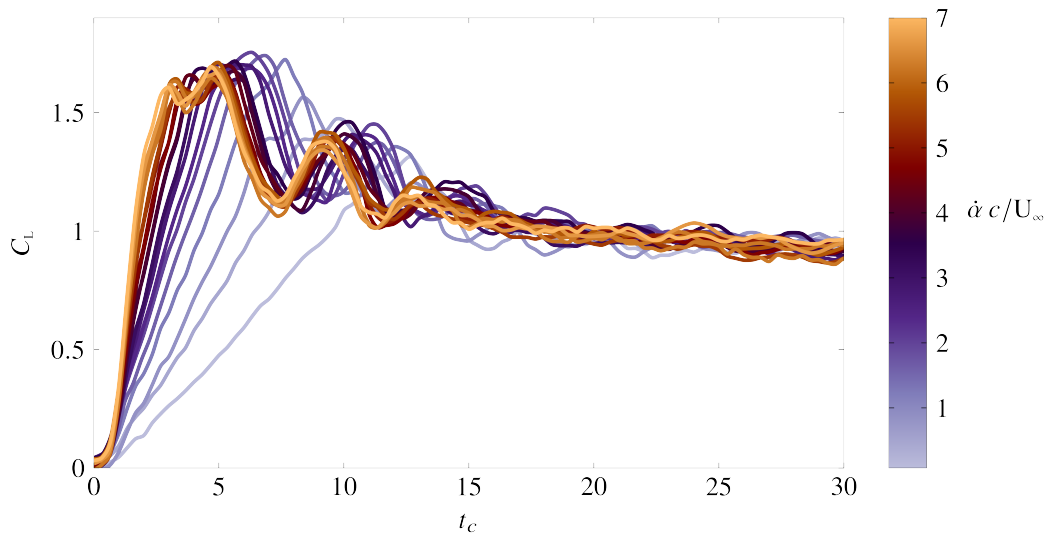


Figure 6 Temporal evolution of the lift coefficient over convective time for dimensionless pitch rates $\dot{\alpha}c/U_\infty$ ranging from 0.75 to 7.5.

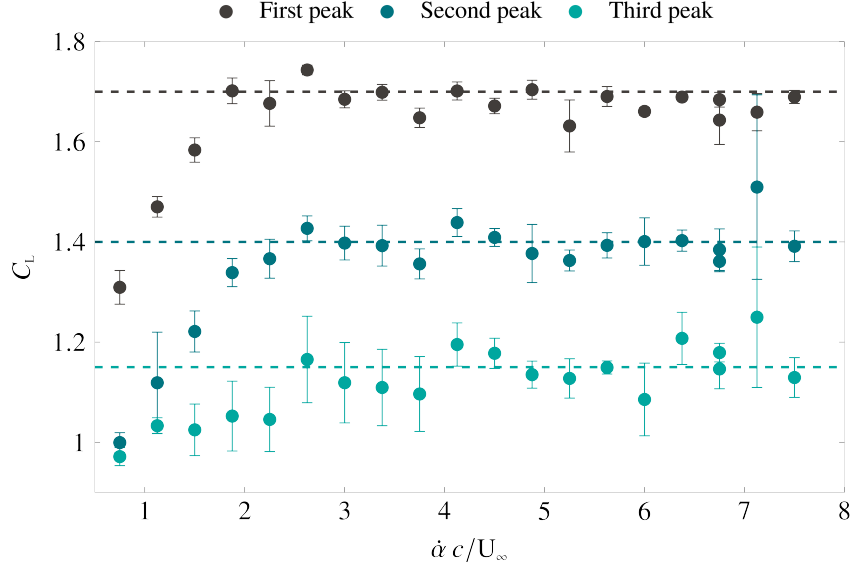


Figure 7 Magnitude of local lift coefficient maxima versus the dimensionless pitch rate.

low pitch rates.

The timing between the first and the second and the second and the third maxima are constant and independent of the pitch rate for all dimensionless pitch rates. The convective time delay between the start of the motion and the first peak is ≈ 5 for high pitch rates, the convective time delay between the first and the second peak is ≈ 4.5 and it decreases further to ≈ 4 between the second and the third peak. This means that the vortex shedding frequency or Strouhal number slight increases for the subsequent shedding cycles until reaching the limit cycle oscillation value.

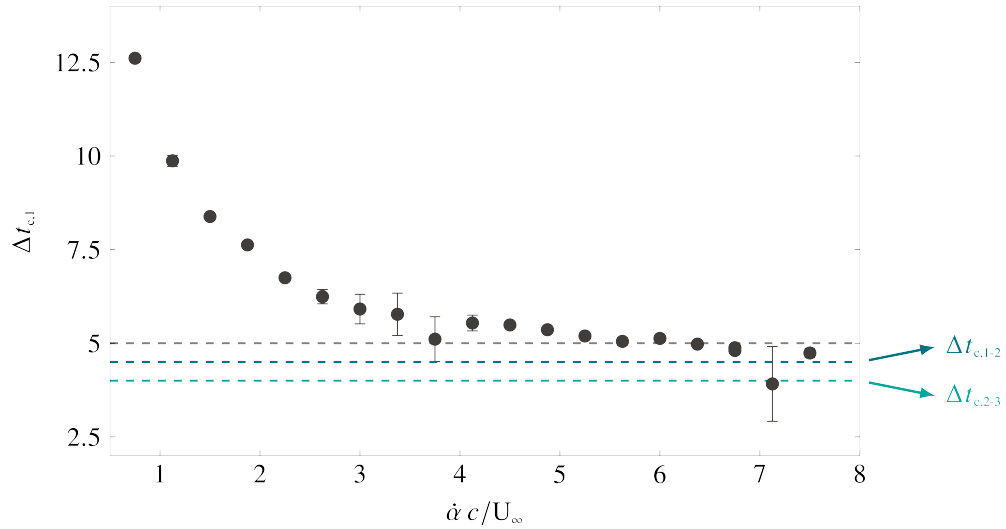


Figure 8 Convective time between the start of the motion and the first lift maximum versus the dimensionless pitch rate.

IV. Conclusion

In this paper, we presented recent activities and results of dynamically stalling airfoils that have been presented at the meetings of the NATO AVT-282 discussion group on *Unsteady aerodynamic response of rigid wings in gust encounters* during the past three years. The three experimental data sets presented include time-resolved PIV and airfoil surface pressure measurements for a sinusoidally pitching OA209 airfoil at $Re = 9.2 \times 10^5$ and for a sinusoidally pitching NACA0015 airfoil profile with an oscillating trailing edge flap at $Re = 5.5 \times 10^5$ and time-resolved PIV and global load measurements for a sharp-edged flat plate undergoing a ramp-up motion in a recirculating water channel at $Re = 77\,500$. Based on the first experimental data, we proposed an improved model of the leading edge suction parameter has been described in more detail in a recent paper by Deparday and Mulleners [10]. The model is based on thin airfoil theory and links the evolution of the leading edge suction and the shear layer during stall development. By taking into account the influence of the shear layer development in terms of a change in the effective angle of attack and effective camber, the new model of the leading edge suction parameter accurately predicts the value and the timing of the maximum leading edge suction on the pitching airfoil.

To further explore the potential of the leading edge suction parameter for identifying and predicting stall onset, we conducted new dynamic stall experiments with a NACA0015 equipped with an oscillating trailing edge flap. By varying the phase delay between the oscillation of the main airfoil and the oscillation of the flap, we were able to influence the stagnation point independent of the velocity of the airfoil's leading edge. By doing so, we can study the role and interaction of the leading edge suction and the leading edge stagnation point. Preliminary results from this data set indicate that the stall delay is only marginally influenced by the flap deflection and motion but the lift polars and the evolution of the leading edge stagnation point are highly influence by the flap kinematics. The stagnation point location is mainly influenced by the instantaneous deflection of the flap. The lift response is not only affected by the instantaneous flap deflection but also by the time history of the flap motion.

With the third experiment, we focus our attention to the load fluctuations that follow dynamic stall onset. For a flat plate that is subjected to a linear ramp up motion, the lift increases linearly until it reached its maximum value which is well above the static stall limit of the flat plate. Additional lift peaks are observed following full stall. These lift peaks subsequently decrease in magnitude and the timing between them is independent of the pitch rate of the initial motion. The magnitude of the lift maximum and the subsequent post stall peak values increase with increasing pitch rate up to a critical pitch rate beyond which the entire lift response become independent of the pitch rate. The convective time delay to reach the primary lift peak decreases with increasing pitch rate up to the critical pitch rate and the time delay between subsequent peaks slightly decreases until the limit cycle oscillation period is reached.

Acknowledgments

We thank the members of the NATO AVT-282 discussion group on *Unsteady aerodynamic response of rigid wings in gust encounters* for the open and fruitful discussions during the various meetings. Special thanks go to the two chairs of the discussion group, Oksan Cetiner and Anya Jones, for leading the discussion group and for organising the meetings and the special session at Scitech 2020.

The work presented is supported by the SNSF Lead Agency programme under grant number 200021E-169841 and by the SNSF Assistant Professor energy grant number PYAPP2_173652.

References

- [1] McCroskey, W. J., and Fisher, R. K., "Dynamic Stall of Airfoils and Helicopter Rotors," Tech. rep., AGARD, 1972.
- [2] Laneville, A., and Vittecoq, P., "Dynamic Stall: The Case of the Vertical Axis Wind Turbine," *Journal of Solar Energy Engineering*, Vol. 108, No. 2, 1986, pp. 140–145.
- [3] Perrotta, G., and Jones, A. R., "Unsteady forcing on a flat-plate wing in large transverse gusts," *Experiments in Fluids*, Vol. 58, No. 8, 2017, p. 101.
- [4] Shih, C., Lourenco, L., Van Dommelen, L., and Krothapalli, A., "Unsteady Flow Past an Airfoil Pitching at a Constant Rate," *AIAA Journal*, Vol. 30, No. 5, 1992, pp. 1153–1161.
- [5] Spentzos, A., Barakos, G. N., Badcock, K., Richards, B., Wernert, P., Schreck, S. J., and Raffel, M., "Investigation of Three-Dimensional Dynamic Stall Using Computational Fluid Dynamics," *AIAA Journal*, Vol. 43, No. 5, 2005, pp. 1023–1033.

- [6] Morris, W. J., and Rusak, Z., “Stall onset on aerofoils at low to moderately high Reynolds number flows,” *Journal of Fluid Mechanics*, Vol. 733, 2013, pp. 439–472.
- [7] Mulleners, K., and Raffel, M., “The onset of dynamic stall revisited,” *Experiments in Fluids*, Vol. 52, No. 3, 2012, pp. 779–793. doi:10.1007/s00348-011-1118-y.
- [8] Mulleners, K., and Raffel, M., “Dynamic stall development,” *Experiments in Fluids*, Vol. 54, No. 2, 2013, pp. 1469–1477.
- [9] Ansell, P., and Mulleners, K., “Multi-scale vortex characteristics of dynamic stall from empirical mode decomposition,” *AIAA Journal*, 2019, pp. 1–18.
- [10] Deparday, J., and Mulleners, K., “Modeling the interplay between the shear layer and leading edge suction during dynamic stall,” *Physics of Fluids*, Vol. 31, No. 10, 2019, p. 107104. doi:10.1063/1.5121312.
- [11] Katz, J., and Plotkin, A., *Low-Speed Aerodynamics*, 2nd ed., Cambridge Aerospace Series, Cambridge University Press, 2004.
- [12] Ramesh, K., Gopalarathnam, A., Granlund, K., Ol, M. V., and Edwards, J. R., “Discrete-vortex method with novel shedding criterion for unsteady aerofoil flows with intermittent leading-edge vortex shedding,” *Journal of Fluid Mechanics*, Vol. 751, 2014, pp. 500–538. doi:10.1017/jfm.2014.297.
- [13] Ramesh, K., Granlund, K., Ol, M. V., Gopalarathnam, A., and Edwards, J. R., “Leading-edge flow criticality as a governing factor in leading-edge vortex initiation in unsteady airfoil flows,” *Theoretical and Computational Fluid Dynamics*, Vol. 32, No. 2, 2018, pp. 109–136.